applied sciences

MDPI

Article

Hydrodynamic Simulation of the Semi-Submersible Wind Float by Investigating Mooring Systems in Irregular Waves

Yu-Hsien Lin * and Cheng-Hao Yang

Department of Systems and Naval Mechatronic Engineering, National Cheng Kung University, Tainan City 70101, Taiwan; dadaorange12345@gmail.com

* Correspondence: vyhlin@mail.ncku.edu.tw; Tel.: +886-6-2757575-63542

Received: 26 May 2020; Accepted: 19 June 2020; Published: 22 June 2020

Abstract: The present study aims to implement the software ANSYS AQWA to discuss the hydrodynamic analysis of the DeepCwind semi-submersible floating platform in waves based on the potential flow theory by considering the second-order wave exciting force. In this study, the linearized potential-flow hydrodynamic radiation and diffraction problems in the frequency domain were firstly solved by adopting the three-dimensional panel method. Subsequently, the hydrodynamic coefficients and wave loading data were transformed to time domain forms by the Cummins time domain equation as a system loading input. Furthermore, the quadratic transfer function (QTF) matrices with different frequencies and directions deduced based on the near field integration over the mean wetted hull surface were adopted for the calculation of slow-drift forces. In order to represent the damping in a real system for modeling potential flow without Morison's elements, an additional quadratic damping matrix was added to capture the viscous drag. Eventually, both of the dynamic mooring model based on the lump-mass (LM) approach and the quasi-static mooring model based on the multi-segmented, quasi-static (MSQS) approach are introduced to discuss the mooring effect on the platform hydrodynamics. The effect of wave heading angles on the platform motion is considered as an influential parameter as well.

Keywords: second-order wave exciting force; dynamic mooring model; quasi-static mooring model; slow-drift force; viscous drag

1. Introduction

Floating offshore wind turbines (FOWTs) have become more important in the global market in recent years due to the increasing demand for wind power. Compared to onshore wind turbines, there are many advantages of FOWTs, including lower noise and higher wind speeds [1]. However, the installation of FOWTs is more difficult because of the cost of construction and the necessity of a more developed offshore wind farm technology [2]. Furthermore, floating wind turbines cannot suffer critical and sudden wave loads, which may cause capsizing. In addition to buoyancy, wind floats also utilize several mooring lines for stabilization. Butterfield et al. [3] mentioned that the classification system used to achieve static stability divides all platforms into three general categories: ballast stabilized, mooring lines stabilized, and buoyancy stabilized. For semi-submersibles, buoyancy is the dominant factor of stability by taking advantage of the weighted water plane area for righting moment, which means mooring lines are the minor factor of stability [4].

Although mooring lines are not the principal factor of stability for platforms, the restoring force provided by mooring lines cannot be ignored. Borg et al. [5] indicated that the analysis of restoring forces due to mooring lines can be calculated using force-displacement-velocity (FDV)

or quasi-static methods. In this method, the quasi-static mooring model involves an analytical derivation of the mooring line tensions. The mooring force consists of the pre-tension force and the linearized mooring force [6]. The pre-tension force is measured using excess buoyancy when the platform is un-displaced. The linearized mooring force can be initially analyzed by the restoring matrix. Nevertheless, the linearized mooring force is not realistic in nature because the mooring systems in most cases are nonlinear. Thomsen et al. [7] indicated that the tension calculated by the quasi-static mooring model could be overestimated in the operational sea condition, but would be underestimated in the severe sea condition. To improve accuracy, there is an expansion of the quasi-static model called the multi-segmented, quasi-static (MSQS) model. Masciola et al. [8] clarified that MSQS allows one to model the nonlinear stiffness matrix and static forces of practical mooring systems with arbitrary connection geometries and profiles. Combining several individual catenary cables, the MSQS model has established the foundation for dynamic mooring analysis.

The dynamic mooring model uses discretization along the cable length and an assembly of the mass and internal forces, which is called the lumped mass method (LMM) [9]. The mooring lines are modeled as a chain of Morison-type elements. Each cable element considers tension force, shear force, and the bending moment. Because the hydrodynamic forces on each cable element are time-variant, the dynamic mooring model is more accurate than the quasi-static mooring model theoretically. In addition, the seabed in the dynamic model is comprised of nonlinear springs and dampers for minimizing discontinuities and energy losses due to the discretization.

According to our previous research [10], the modular simulation system is well developed and can be used to estimate hydrodynamic forces for different types of floating offshore wind turbines with the quasi-static mooring lines in waves. Furthermore, this study attempts to represent the hydrodynamic coefficients and the motion responses of the semi-submersible using a numerical simulation based on the linear potential flow theory and the assumption of the 2nd order wave exciting force. Compared to the dynamic mooring system, the motion responses of a platform moored using quasi-static cables are discussed in detail. The simulation results will be compared with published data for verifying accuracy as well.

2. Mathematical Model

2.1. Structure of Semi-Submersibles

This study applies the semi-submersible floating offshore wind system in the Offshore Code Comparison Collaboration Continuation (OC4) project [11] to numerical simulation. The floating platform is composed of two parts, i.e., three pontoons and one main column attached to the tower, and each part is connected by several cross braces. Furthermore, there are three mooring lines connecting to the base columns for stabilizing the floating platform. The design and three-view drawing of the semi-submersible floating offshore wind system are shown in Figure 1a,b.

2.2. Coordinate System

The earth-fixed coordinate system O_0-$X_0Y_0Z_0$, shown in Figure 2, has its origin in the mean free surface, i.e., $Z_0 = 0$, with the Z_0-axis pointing vertically upwards, and the X_0-axis denotes wave incidence; ω is denoted as wave angular frequency; wave incident angle $\theta = 0^\circ$ represents wave propagation in the positive X_0 direction; h is defined as the water depth. The body-fixed coordinate system is able to define the free surface boundary condition. The position of the origin is fixed at the center of gravity (COG) and changes along with transition or rotation of the floating body.

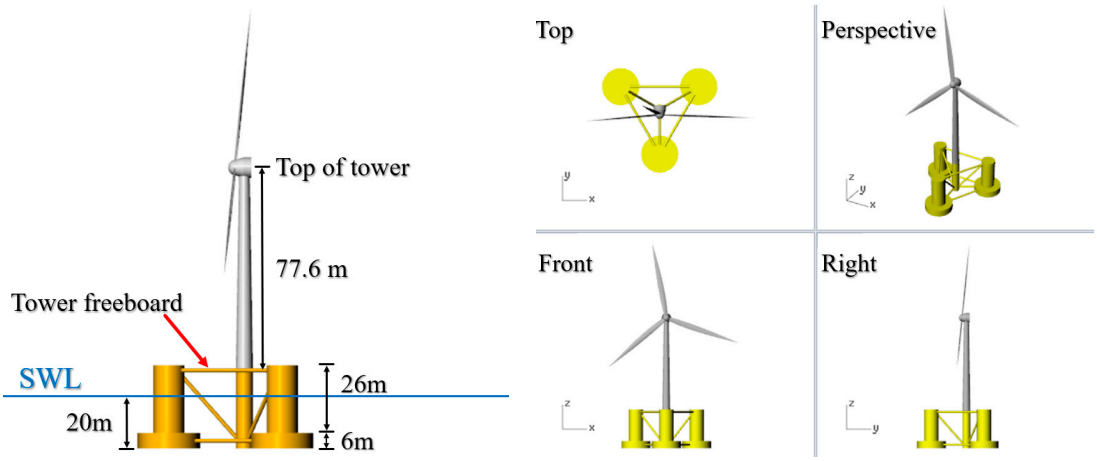

Figure 1. The schematic diagram: (**a**) the design, and (**b**) three-view drawing of the semi-submersible.

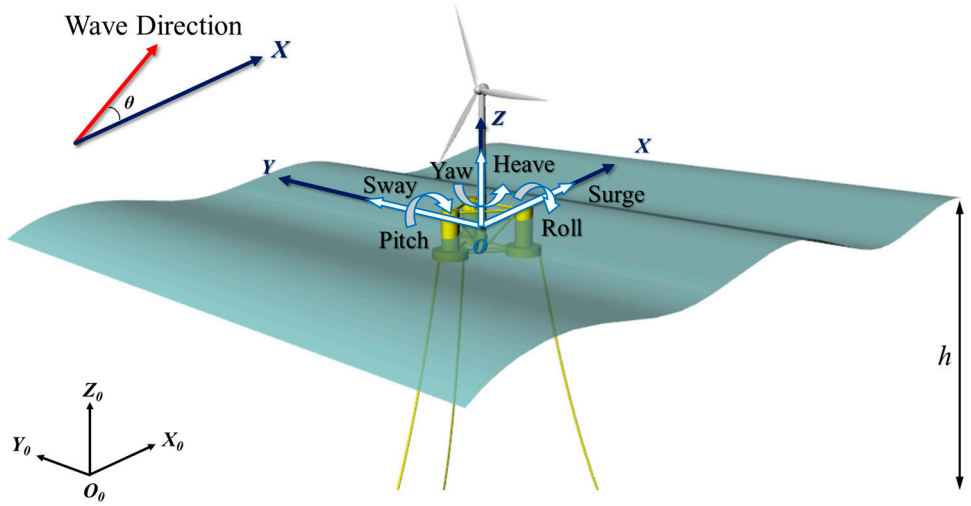

Figure 2. The diagrams of earth-fixed (O_0-$X_0Y_0Z_0$) and body-fixed (O-XYZ) coordinate systems.

2.3. *Potential Flow Theory*

2.3.1. Linear Potential Flow Theory

Linear potential flow theory is used to solve the radiation and diffraction problems. It is assumed that the water around the floating structure is a Newtonian fluid, which is irrotational, incompressible, and inviscid. Since the potential velocity ϕ satisfies the boundary conditions and Laplace equation, the total velocity potential can be written as:

$$\phi(x,\ y,\ z,\ t) = \phi_I(x,\ y,\ z,\ t) + \phi_D(x,\ y,\ z,\ t) + \sum_{j=1}^{6} \zeta_j \phi_{R_j}(x,\ y,\ z,\ t) \tag{1}$$

where $\phi_I(x,\ y,\ z,\ t)$ is the incident wave potential; $\phi_D(x,\ y,\ z,\ t)$ is the diffraction wave potential; $\phi_{R_j}(x,\ y,\ z,\ t)$ is the radiation wave potential; ζ_j represents motion displacement; and $j = 1, 2, \ldots, 6$ represents surge, sway, heave, roll, pitch and yaw, respectively.

The incident wave potential $\phi_I(x,\ y,\ z,\ t)$ can be expressed as:

$$\phi_I(x,\ y,\ z,\ t) = \frac{-iga}{\omega_o} e^{k_0 z} e^{i(k_0 x cos\theta + k_0 y sin\theta - \omega_0 t)} \tag{2}$$

where i is the imaginary unit; a is the incident wave amplitude; g is gravity; k_0 is the wave number; and θ is the angle of wave incidence.

The diffraction wave potential $\phi_D(x,\ y,\ z,\ t)$ can be expressed as:

$$\phi_D(x,\ y,\ z,\ t) = e^{ik_0 x \cos\theta - \omega_0 t} \int_C Q(\eta,\ \zeta) G(y,\ z,\ \eta,\ \zeta;\ k_0) dC \tag{3}$$

where the Green function G is the two-dimensional pulsating source potential of intensity at the point $(\eta,\ \zeta)$ in the lower half of the y−z plane; and C indicates that the integral is to be taken along the hull-section contour below the calm water surface.

The first order exciting force $F^{(1)}$ in i-th mode can be derived from the following equation by adopting the incident and diffraction potentials:

$$F^{(1)} = -i\rho_w \omega \iint_s [\phi_I(x,\ y,\ z,\ t) + \phi_D(x,\ y,\ z,\ t)] \cdot n_i(x,\ y,\ z,\ t) dS \tag{4}$$

where ρ_w is seawater density; S is the wetted body surface of the floating body; and n_i is the i-th mode normal vector on the wetted body surface.

The i-th mode radiation force $\zeta_j \phi_R$ can be derived from the following equation by adopting the radiation potentials:

$$F_i^R \zeta_j = i\rho_w \omega \iint_s \sum_{j=1}^{6} \zeta_j \phi_{Rj} \cdot n_i dS = \sum_{j=1}^{6} \left(\omega^2 \mu_{ij} + i\omega \nu_{ij}\right) \zeta_j,\ i = 1,\ 2,\ \ldots,\ 6 \tag{5}$$

$$\mu_{ij} = -\rho_w \omega \iint_s \phi_{Rj} \cdot n_i dS \tag{6}$$

$$\nu_{ij} = -\rho_w \omega \iint_s \phi_{Rj} \cdot n_i dS \tag{7}$$

where μ_{ij} is the added mass coefficient; and ν_{ij} is the damping coefficient.

2.3.2. Second-Order Wave Excitation Force

In order to predict second-order (2nd) wave exciting forces, the equations of velocity potential, wave elevation, and the position of a floater can be expanded as follows:

$$\phi = \varepsilon \phi^{(1)} + \varepsilon^2 \phi^{(2)} + O\left(\varepsilon^3\right),\ \text{where } \varepsilon \to 0 \tag{8}$$

$$\zeta = \zeta^{(0)} + \varepsilon \zeta^{(1)} + \varepsilon^2 \zeta^{(2)} + O\left(\varepsilon^3\right),\ \text{where } \varepsilon \to 0 \tag{9}$$

$$\vec{X} = \vec{X}^{(0)} + \varepsilon \vec{X}^{(1)} + \varepsilon^2 \vec{X}^{(2)} + O\left(\varepsilon^3\right),\ \text{where } \varepsilon \to 0 \tag{10}$$

where ϕ is the velocity potential; ζ is the wave elevation; $\vec{X}$ is the position of the floater; the superscript (0) represents the static values; and the superscripts (1) and (2) represent the 1st and the 2nd order variations with respect to the perturbation parameter ε.

The estimation of the 2nd wave exciting force is based on the perturbation method [12]. The 2nd wave exciting force and moment can be expressed as:

$$\begin{aligned}\vec{F}^{(2)} = & -\tfrac{1}{2}\rho_w g \oint_{WL} \zeta_r{}^{(1)}\cdot\zeta_r{}^{(1)}\vec{n}\,dl \\ & +\tfrac{1}{2}\rho_w \iint_{S_0}\left[\nabla\phi^{(1)}\cdot\nabla\phi^{(1)}\right]\vec{n}\,dS + \rho_w \iint_{S_0}\left[\vec{X}^{(1)}\cdot\nabla\frac{\partial\phi^{(1)}}{\partial t}\right]\vec{n}\,dS + \vec{\alpha}^{(1)}\times\vec{F}^{(1)} \\ & +\rho_w \iint_{S_0}\frac{\partial\phi^{(2)}}{\partial t}\vec{n}\,dS\end{aligned} \tag{11}$$

$$\begin{aligned}\vec{M}^{(2)} = & -\tfrac{1}{2}\rho_w g \oint_{WL} \zeta_r{}^{(1)}\cdot\zeta_r{}^{(1)}\left(\vec{x}\times\vec{n}\right)dl \\ & +\tfrac{1}{2}\rho_w \iint_{S_0}\left[\nabla\phi^{(1)}\cdot\nabla\phi^{(1)}\right]\left(\vec{x}\times\vec{n}\right)dS + \rho_w \iint_{S_0}\left[\vec{X}^{(1)}\cdot\nabla\frac{\partial\phi^{(1)}}{\partial t}\right]\left(\vec{x}\times\vec{n}\right)dS \\ & +\vec{\alpha}^{(1)}\times\vec{M}^{(1)} + \rho_w \iint_{S_0}\frac{\partial\phi^{(2)}}{\partial t}\left(\vec{x}\times\vec{n}\right)dS\end{aligned} \tag{12}$$

where $\zeta_r{}^{(1)}\left(=\zeta^{(1)} - X_{3\,WL}^{(1)}\right)$ is the relative wave elevation along the mean undisturbed water line; $\zeta^{(1)}$ is the wave elevation; $X_{3\,WL}^{(1)}$ is the vertical distance of the point below the free surface; WL represents the undisturbed water line; $\vec{\alpha}^{(1)}$ is the 1st order rotational motion of the center of gravity in the fixed reference axes; S_0 is the mean wetted surface; dS and dl denote the surface element and the length element of the waterline; $\vec{n}$ is the normal vector of a length element dl; $\vec{F}^{(1)}$ and $\vec{M}^{(1)}$ are the total 1st order fluid force and moment; and $\vec{\alpha}^{(1)}$ is the 1st order rotational motion vector.

In order to simplify the 2nd order wave exciting force, the quadratic transfer function (QTF) was applied in the hydrodynamic force analysis. Considering a pair of the regular incident waves with $\left(a_{jm},\ \omega_{jm},\ x_m,\ \alpha_{jm}\right)$ and $(a_{kn},\ \omega_{kn},\ x_n,\ \alpha_{kn})$, the interaction of two waves results in the 2nd order wave exciting force due to the difference or the sum frequency. The 2nd order wave exciting force with QTF matrices in the time domain can be expressed as:

$$\begin{aligned}\vec{F}^{(2)} = & \sum_{m=1}^{N_d}\sum_{n=1}^{N_d}\sum_{j=1}^{N_m}\sum_{k=1}^{N_n} a_{jm}a_{kn}\{\vec{P}^{+}_{jkmn}\cos\left[\left(\omega_{jm}+\omega_{kn}\right)t-\left(\alpha_{jm}+\alpha_{kn}\right)\right] \\ & +\vec{Q}^{+}_{jkmn}\sin\left[\left(\omega_{jm}+\omega_{kn}\right)t-\left(\alpha_{jm}+\alpha_{kn}\right)\right] \\ & +\vec{P}^{-}_{jkmn}\cos\left[\left(\omega_{jm}-\omega_{kn}\right)t-\left(\alpha_{jm}-\alpha_{kn}\right)\right] \\ & +\vec{Q}^{-}_{jkmn}\sin\left[\left(\omega_{jm}-\omega_{kn}\right)t-\left(\alpha_{jm}-\alpha_{kn}\right)\right]\}\end{aligned} \tag{13}$$

where $(\vec{P}^{+}_{jkmn}, \vec{Q}^{+}_{jkmn})$ and $(\vec{P}^{-}_{jkmn}, \vec{Q}^{-}_{jkmn})$ represent in-phase and out-of-phase components of sum and difference frequency forces/moments. $\vec{P}^{+'}_{jkmn}$, $Q^{+'}_{jkmn}$, and $\vec{P}^{-'}_{jkmn}$ are symmetric against a pair of waves with $\left(a_{jm},\omega_{jm},\chi_{jm},\alpha_{jm}\right)$ and $(a_{km},\omega_{km},\chi_{km},\alpha_{km})$. On the other hand, $\vec{Q}^{-'}_{jkmn}$ is skew-symmetric against this pair of waves. N_d is the number of wave directions; and N_m and N_n are the numbers of wave components in the m-th and the n-th wave directions.

For the purpose of establishing a more simplified equation, the sum and difference frequency components are defined as below:

$$\vec{P}^{+'}_{jkmn} = \frac{1}{2}\left(\vec{P}^{+}_{jkmn} + \vec{P}^{+}_{kjmn}\right) = \vec{P}^{+'}_{kjmn} \tag{14}$$

$$Q^{+'}_{jkmn} = \frac{1}{2}\left(\vec{Q}^{+}_{jkmn} + \vec{Q}^{+}_{kjmn}\right) = \vec{Q}^{+'}_{kjmn} \tag{15}$$

$$\vec{P}^{-'}_{jkmn} = \frac{1}{2}\left(\vec{P}^{-}_{jkmn} + \vec{P}^{-}_{kjmn}\right) = \vec{P}^{-'}_{kjmn} \tag{16}$$

$$\vec{Q}^{-'}_{jkmn} = \frac{1}{2}\left(\vec{Q}^{-}_{jkmn} - \vec{Q}^{-}_{kjmn}\right) = Q^{-'}_{kjmn} \tag{17}$$

Applying the above definitions, Equation (13) can be rewritten as below:

$$\begin{aligned} \vec{F}^{(2)} = \sum_{m=1}^{N_d}\sum_{n=1}^{N_d}\sum_{j=1}^{N_m}\sum_{k=1}^{N_n} a_{jm}a_{kn}\{ & \vec{P}^{+'}_{jkmn}\cos\left[\left(\omega_{jm}+\omega_{kn}\right)t - \left(\alpha_{jm}+\alpha_{kn}\right)\right] \\ & + \vec{Q}^{+'}_{jkmn}\sin\left[\left(\omega_{jm}+\omega_{kn}\right)t - \left(\alpha_{jm}+\alpha_{kn}\right)\right] \\ & + \vec{P}^{-'}_{jkmn}\cos\left[\left(\omega_{jm}-\omega_{kn}\right)t - \left(\alpha_{jm}-\alpha_{kn}\right)\right] \\ & + \vec{Q}^{-'}_{jkmn}\sin\left[\left(\omega_{jm}-\omega_{kn}\right)t - \left(\alpha_{jm}-\alpha_{kn}\right)\right]\} \end{aligned} \tag{18}$$

2.4. Mooring System Modelling

2.4.1. Quasi-Static Mooring Model

The quasi-static mooring model shown in Figure 3a applies the multi-segmented, quasi-static (MSQS) approach [8] to obtain the mooring force. Each mooring force consists of two parts, including the pre-tension and linearized mooring force. The total mooring force is the sum of each mooring force.

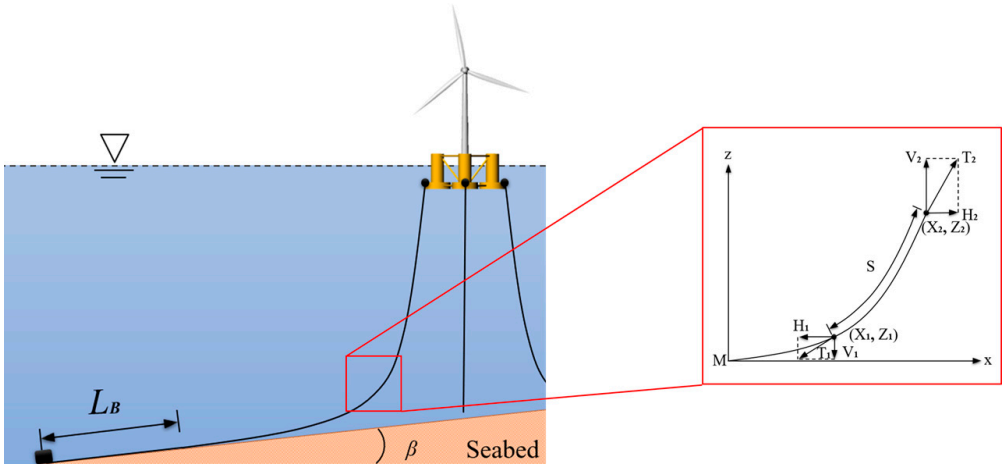

(**a**) (**b**)

Figure 3. Description of the quasi-static mooring model: (**a**) the schematic diagram of quasi-static model; (**b**) the catenary solution of each quasi-static mooring line. L_B means the length of the un-stretched mooring cable on the seabed; β is the slope of seabed; and S is the un-stretched length of a catenary segment from its top right end $(X_2,\ Z_2)$.

Figure 3b shows the catenary solution of each quasi-static mooring line. Hasselmann et al. [13] derived the solution of the catenary equation for a single line. The motion equation of each catenary section can be expressed as follows:

$$H_2 = AE\sqrt{\left(\frac{T_2}{AE}+1\right)^2 - \frac{2wZ_2}{AE}} - AE \tag{19}$$

$$X_2 = \frac{H_2}{w}\sinh^{-1}\left(\frac{wL}{H_2}\right) + \frac{H_2 L}{AE} \tag{20}$$

$$V_2 = wL \tag{21}$$

$$T_2 = \sqrt{{H_2}^2 + {V_2}^2} \tag{22}$$

where L is the un-stretched suspend length from the origin to the point $(X_2,\ Z_2)$; w is the submerged weight per unit length; T_1 and T_2 represent the tension force; V_1 and V_2 denote the vertical component of the tension force; H_1 and H_2 mean the horizontal component of the tension force; and AE is the stiffness per unit length.

In addition, the stretched length of the suspended catenary mooring line can be expressed as:

$$L' = L + \frac{1}{2wAE}\left\{wL\sqrt{H^2 + (wL)^2} + H^2 ln\left[wL + \sqrt{H^2 + (wL)^2}\right] - H^2 ln|H|\right\} \tag{23}$$

Given that the un-stretched length of a catenary segment from its top right end $(X_2,\ Z_2)$ is S, S is shorter than the theoretical un-stretched suspended length S. When the tension force at the top right end is known, the position of the bottom left end of this segment can be written as:

$$X_1 = \frac{H}{w} ln \frac{V_2 + T_2}{V_1 + T_1} + \frac{HS}{AE} \tag{24}$$

$$Y_1 = \frac{V_2 + V_1}{T_2 + T_1} S + \frac{V_2 + V_1}{2AE} S \tag{25}$$

The horizontal and vertical components of the tension forces at the left-hand end are

$$H_1 = H \tag{26}$$

$$V_1 = V_2 - wS \tag{27}$$

$$T_1 = \sqrt{H_1^2 + T_1^2} \tag{28}$$

In addition, the stretched length of the catenary segment is defined as:

$$S' = S + \frac{1}{2wAE}\left(V_2 T_2 - V_1 T_1 + H^2 ln \frac{V_2 + T_2}{V_1 + T_1}\right) \tag{29}$$

Finally, the mooring force F_M obtained from the quasi-static mooring model is simply represented as:

$$F_M = T_2 - T_1 \tag{30}$$

2.4.2. Dynamic Mooring Model

In the dynamic mooring model, the lumped-mass method [9] is used to calculate the dynamic simulation of the interconnected cables, the weight and the buoyancy. In this method, as shown in Figure 4a, the mooring cable is separated into N equally-sized line segments connecting $N + 1$ node points. The index i starts from the anchoring node at the bottom, in which the value of the anchoring node is given as zero. The index value of the line segment between nodes 0 and 1 is 1/2, and the node at the top of the fairlead node is N.

In the right-handed inertial reference coordinate system, the z-axis is measured in a positive upward direction from the water plane. The position of each node i is defined by the position vector r_i, containing the x, y and z coordinates of the node position. Each mooring line segment $i + \frac{1}{2}$ has the same properties of un-stretched length L, volume-equivalent diameter d, Young's modulus E, and the inertial damping coefficient C_{int}. The dynamic mooring model combines internal stiffness, damping force, weight, buoyancy, hydrodynamic forces from Morison equation, and contact force from the seabed, as illustrated in Figure 4b. The internal stiffness and damping force of the line segment $i + 1/2$

are expressed as $T_{i+(1/2)}$ and $C_{i+(1/2)}$, respectively. Meanwhile, the weight of the line segment lumped at each node i is denoted as W_i, whereas B_i is the net buoyancy at node i.

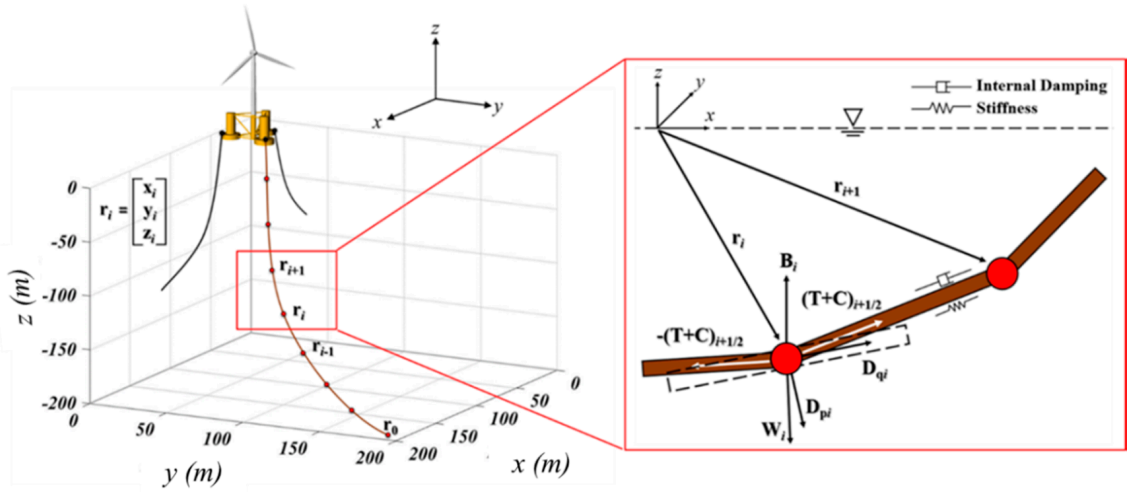

(**a**) (**b**)

Figure 4. Description of dynamic mooring model: (**a**) the discretization of a mooring cable; (**b**) internal and external forces of a dynamic mooring cable.

In the lumped-mass (LM) method, the mass of the mooring cable is discretized into point masses at each node by assigning each node half the combined mass of the two adjacent line segments. The 3×3 mass matrix for node i can be represented by

$$m_i = \frac{\pi}{4} d^2 L \rho I \tag{31}$$

where ρ is the density of the mooring cable; I is the identity matrix.

The added-mass matrix, which is included in the mass matrix, for node i is expressed as

$$a_i = a_{p_i} + a_{q_i} = \rho \frac{\pi}{4} d^2 L \left[C_{an} \left(I - \hat{q}_i \hat{q}_i^T \right) + C_{at} \left(\hat{q}_i \hat{q}_i^T \right) \right] \tag{32}$$

where a_{p_i} and a_{q_i} are the corresponding transverse and tangential added-mass matrices, respectively. C_{an} (=0.865) and C_{at} (=0.269) are added-mass coefficients in the transverse and tangential directions [9,14]. $\hat{q}_i$ is defined as the tangent direction at each node and can be approximated as the direction of a line passing between the two adjacent node points by

$$\hat{q}_i = \frac{r_{i+1} - r_{i-1}}{\| r_{i+1} - r_{i-1} \|} \tag{33}$$

where r_i is the position vector at node i.

Finally, the motion equation of the mooring cable for each node i is

$$\begin{aligned} F_M &= \sum_{i=1}^{N} (m_i + a_i) \ddot{r}_i \\ &= \sum_{i=1}^{N} \left[T_{i+(1/2)} - T_{i-(1/2)} + C_{i+(1/2)} - C_{i-(1/2)} + W_i + B_i + D_{pi} + D_{qi} \right] \end{aligned} \tag{34}$$

where D_{pi} and D_{qi} are drag forces in the transverse and tangential directions, respectively.

2.5. Six-DOF Motion Equations

Substituting the 1st and the 2nd order wave exciting forces as well as other external forces into 6-DOF motion equations, the Cummins time-domain equation [15] can be written as below:

$$\begin{aligned}\{m + A_\infty\}\ddot{\zeta}(t) \quad &= F^{(1)}(t) + F^{(2)}(t) + F_M(t) - c\dot{\zeta}(t) - B|\dot{\zeta}(t)|\dot{\zeta}(t) - K\zeta(t) \\ &\quad - \int_0^t h(t-\tau)\ddot{\zeta}(\tau)d\tau\end{aligned} \tag{35}$$

where $F^{(1)}(t)$ is the 1st order wave excitation force/moment; $F^{(2)}(t)$ is the 2nd order wave excitation force/moment; $F_M(t)$ is the mooring force; c is the linear damping matrix including the linear radiation damping effects; B is the quadratic damping matrix including the equivalent linear damping values to compensate for the viscous and eddy drag effects; K is the total stiffness matrix including the hydrostatic term as well as the stiffness from mooring lines; m is the structural mass; A_∞ is the added mass matrix at the infinite frequency; $h(t)$ is impulse response function; $\zeta(t)$, and $\ddot{\zeta}(t)$ represent the displacement, velocity and acceleration time-series vectors in translational or rotational motions, respectively.

Since the 6-DOF motion responses were calculated in the time domain, the 4th Order Runge–Kutta method was used for numerical simulation [10]. The total time length of each numerical simulation was set to be 8000 s with the time step of 0.1 s.

2.6. Meshing

For solving the hydrodynamic coefficients, the diffraction elements located below the still water level were considered in the simulation. The maximum element size was 1.5 m, and the mesh discretization of the semi-submersible FOWT and wetted meshes is shown in Figure 5a,b, respectively. The detail of mesh settings is presented in Table 1. Subsequently, the grid-independence test will be conducted in Section 4.1.

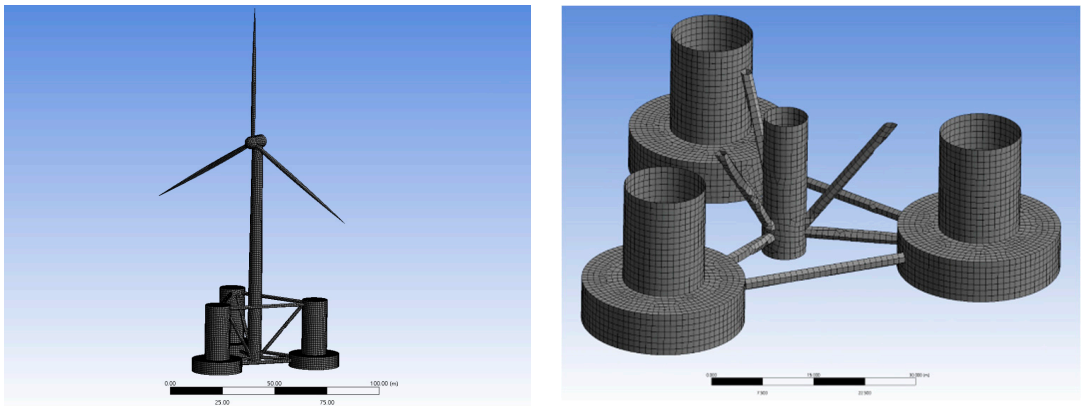

(**a**) (**b**)

Figure 5. The mesh discretization: (**a**) semi-submersible FOWT; and (**b**) semi-submersible platform below the free surface.

Table 1. Detail of mesh settings

Mesh Properties	Value	Unit
Maximum Element Size	1.5	m
Maximum Allowed Frequency	0.449	Hz
Diffracting Nodes	9220	N/A
Diffracting Elements	9227	N/A

3. Mooring Line Properties

To stabilize the floating platform, the mooring lines located at the top of the base columns prevent the platform from capsizing and keep the position in the waves. The mooring layout is introduced in Figure 6, and the mooring line properties are presented in Table 2.

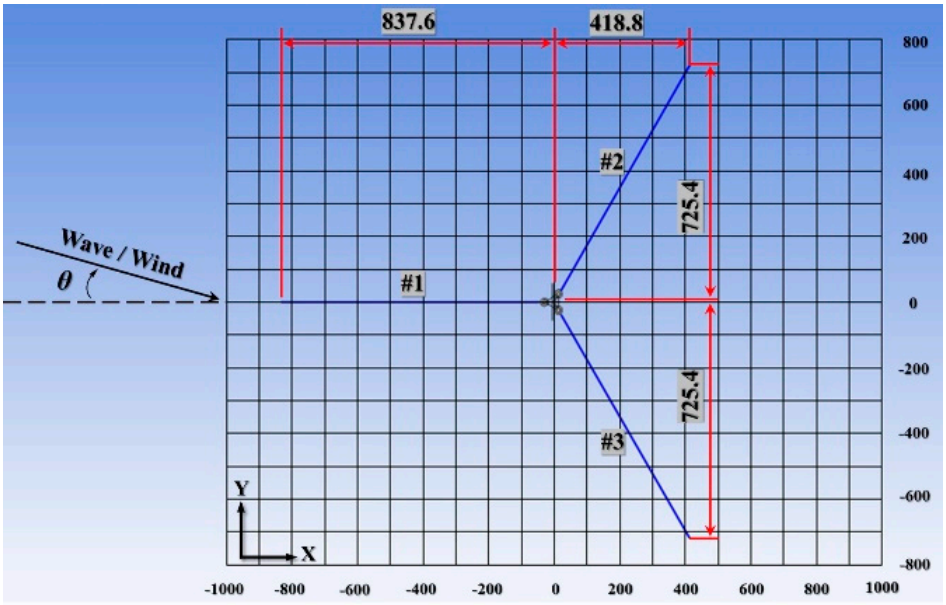

Figure 6. The mooring layout in θ = 0°, 30°, 60°, and 90° wave heading angles.

Table 2. Mooring line properties [11].

Mooring Line Properties	Value	Unit
Number of mooring lines	3	N/A
Angle between adjacent lines θ_M	120	degree
Depth to anchors below SWL	200	m
Depth to fairleads below SWL	14	m
Radius to anchors from platform centerline R_A	837.6	m
Radius to fairleads from platform centerline R_F	40.868	m
Unstretched mooring line length S	835.5	m
Mooring line diameter D_e	0.0766	m
Equivalent mooring line mass density ρ	113.35	kg/m
Equivalent mooring line extensional stiffness K	753.6	MN

4. Results and Discussion

4.1. Analysis of Hydrodynamic Coefficients

The surface of the DeepCwind semi-submersible FOWT is divided into several meshes, which are composed of non-diffracting and diffracting elements. For obtaining the hydrodynamic coefficients, the semi-submersible is under 0-degree waves, and the radiation force on diffracting elements is precisely calculated. With Equation (5), the hydrodynamic coefficients in six modes are thus obtained. The interaction between waves and the semi-submersible FOWT is illustrated in Figure 7.

The added-mass and damping coefficients with five panel numbers was compared to the WAMIT data obtained from University of Ulsan (UOU) [16] in the surge, heave and pitch modes, as illustrated in Figures 8 and 9. In the UOU in-house code, the hydrodynamic coefficients, including added mass, radiation damping and wave exciting forces, of the DeepCwind semi-submersible FOWT were calculated by using a diffraction/radiation solver in the frequency domain. It is noted that the surge-surge elements of the added-mass and damping coefficients, μ_{11} and ν_{11}, are identical to the

sway-sway elements, μ_{22} and ν_{22} due to the symmetry of the DeepCwind semi-submersible FOWT. Furthermore, the roll-roll elements, μ_{44} and ν_{44}, are also identical to the pitch-pitch elements, μ_{55} and ν_{55}. Thus, identical results were assembled in the same plots.

According to the grid-independence test, the difference ratios of 9117 panels and 20,545 panels are less than 1%. Therefore, 9117 panels is enough for the simulation. Additionally, it is obvious in Figures 8 and 9 that the numerical results in both surge and heave modes are close to the WAMIT data, and the peak frequency of these two hydrodynamic coefficients are perfectly met. However, the peak frequencies in the pitch mode slightly deviate from the WAMIT data, which is similar to the findings [17]. The discrepancies between the WAMIT data [16] and our simulation results may be due to the geometric description methods. For WAMIT analysis, a higher-order representation geometric description file, in which the velocity potential on the body surface was represented using B-splines, for the DeepCwind semisubmersible FOWT was created. For our simulation, the un-structured panel grids on most parts of the wetted hull were generated, whereas the structured grids were only distributed on the columns. Even though there are some differences between the numerical results and the WAMIT data, the trends of the hydrodynamic coefficients are similar. The comparison demonstrates that the current 3D panel method is an acceptable calculation for generating the hydrodynamic coefficients required by subsequent time-domain analysis.

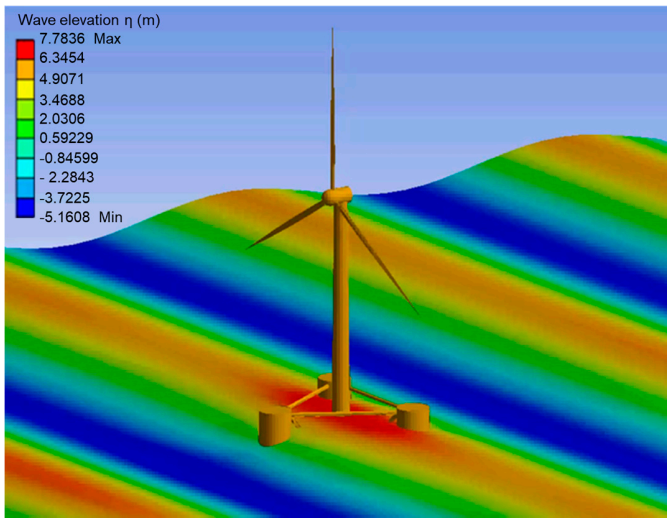

Figure 7. Visualization of the interaction between waves and DeepCwind semi-submersible FOWT.

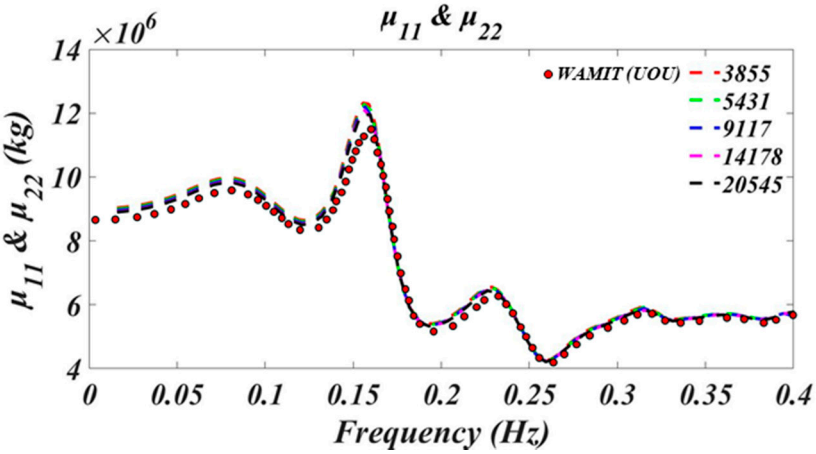

(**a**)

Figure 8. *Cont.*

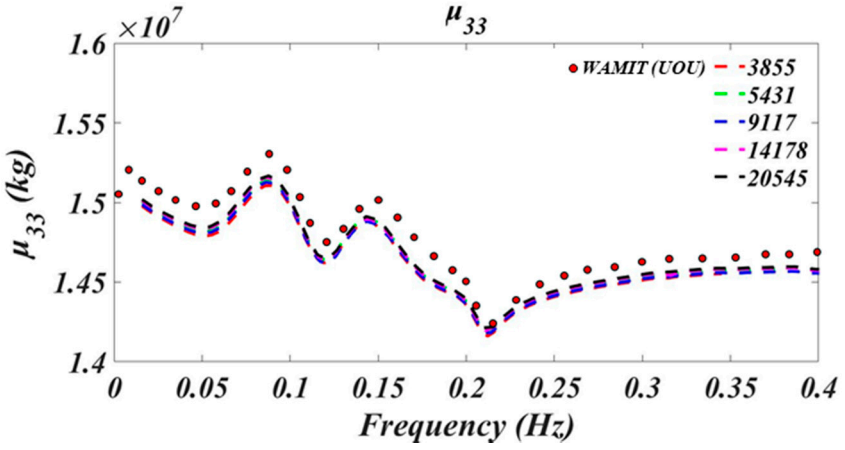

(**b**)

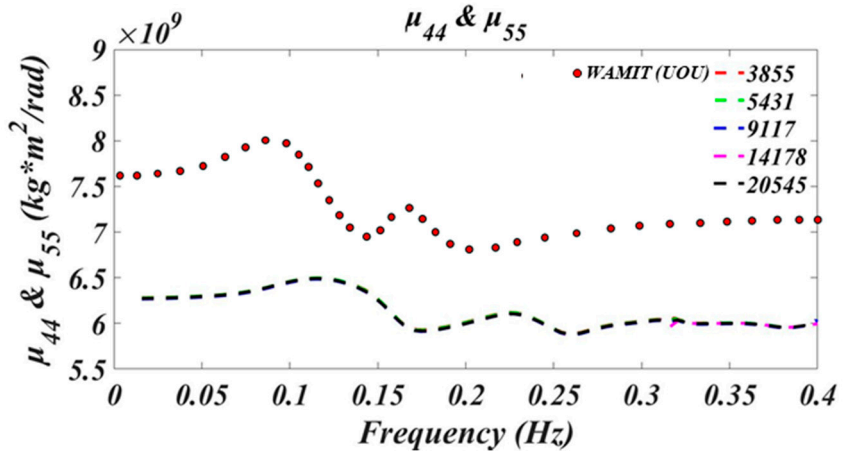

(**c**)

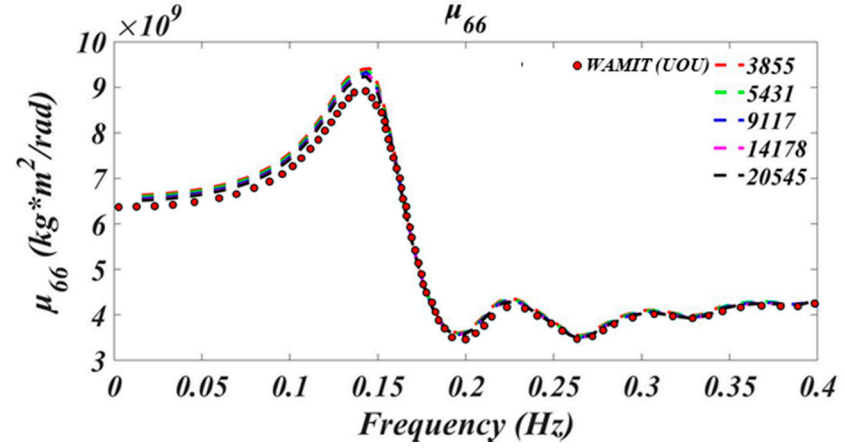

(**d**)

Figure 8. The comparison of added-mass coefficients between different mesh numbers and the UOU data in (**a**) surge and sway, (**b**) heave, (**c**) roll and pitch, and (**d**) yaw modes.

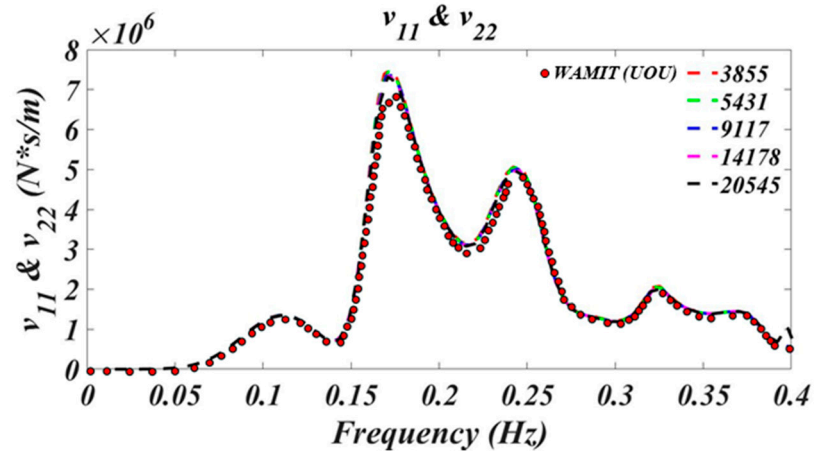

(a)

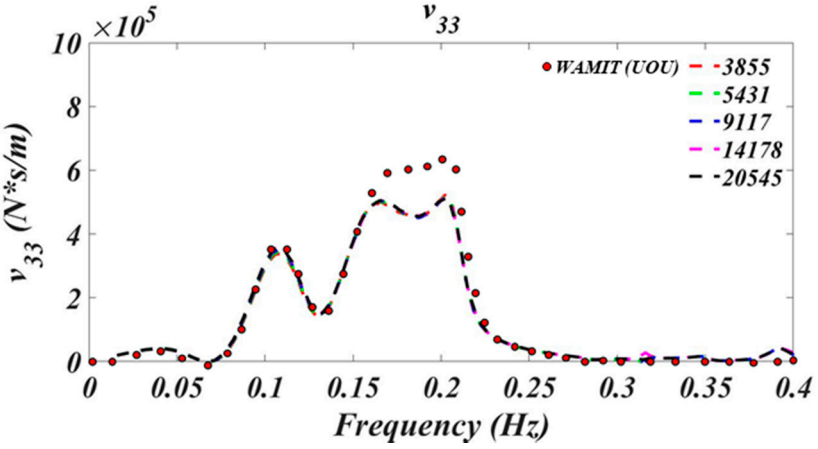

(b)

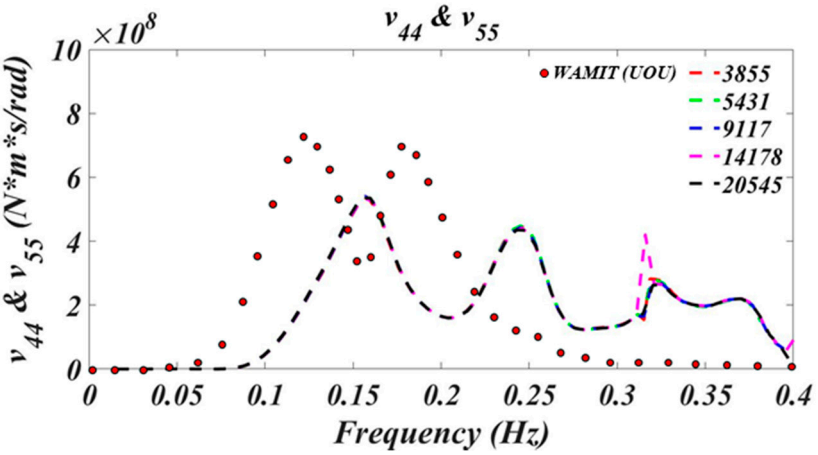

(c)

Figure 9. *Cont.*

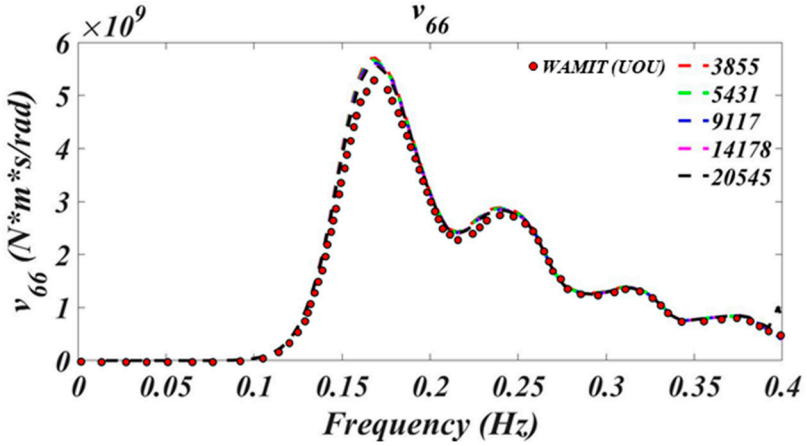

(**d**)

Figure 9. The comparison of damping coefficients between different mesh numbers and the UOU data in (**a**) surge and sway, (**b**) heave, (**c**) roll and pitch, and (**d**) yaw modes

4.2. Wave Spectrum

For the hydrodynamic loads, the time-domain wave excitation for the computation was implemented using a white-noise wave spectrum [18], as illustrated in Figure 10. In the subsequent simulation, each computation was carried out for a time duration of 8000 s with a time step size of 0.1 s. In this study, the response amplitude operator (RAO) was defined as the ratio of the cross-spectral density of the surface elevation (input) and the corresponding system response (output) to the auto-spectral density of the surface elevation, and can be expressed as:

$$RAO = G(\omega) = \frac{S_{xy}(\omega)}{S_{xx}(\omega)} \tag{36}$$

where $G(\omega)$ indicates the frequency response function (FRF) or the RAO; $S_{xx}(\omega)$ and $S_{xy}(\omega)$ are the auto-spectral and cross-spectral densities in the frequency domain.

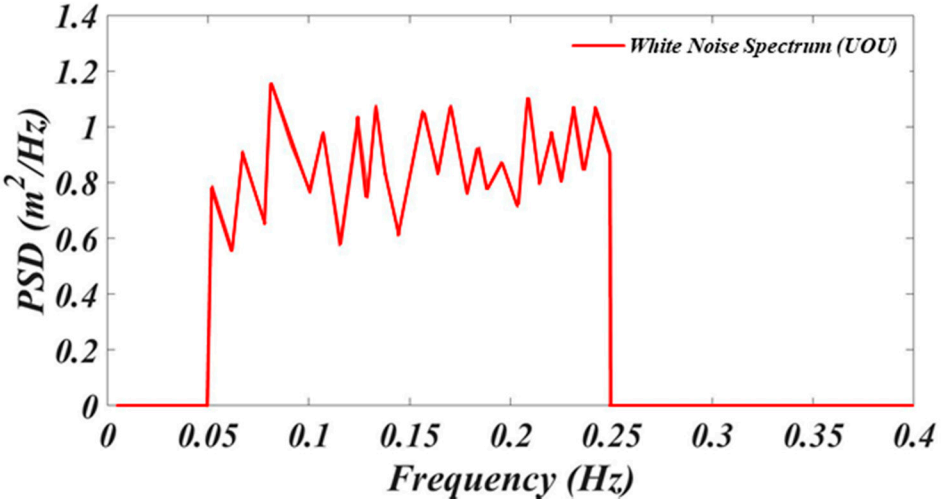

Figure 10. The schematic of the white-noise spectrum.

The post-processing of these computations in the time domain was repeated for different load cases and degrees of freedom. Since the wave energy exists in 0.05 to 0.25 Hz, the RAOs were only

discussed in this frequency region, which was meaningful for investigating the motion response in irregular waves and for code-to-code comparison.

4.3. Load Case

In order to compare the motion responses of DeepCwind semi-submersible FOWT achieved by our model with the results of UOU in-house codes, seven load cases were conducted including different model settings, i.e., potential flow theory, quadratic damping, mooring model, and wave heading angles. Table 3 summarizes all load cases that would be discussed in the following sections. These simulations were executed in the absence of wind force, and with the rotor locked.

Table 3. The description of load cases.

Case Name	Model Description	Wave Heading
UOU	1st Order + QD + QS	0°
LC1	1st Order + QS	0°
LC2	1st Order + QD + QS	0°
LC3	1st Order + QD + QS + QTF	0°
LC4	1st Order + QD + Dyn + QTF	0°
LC5	1st Order + QD + Dyn + QTF	30°
LC6	1st Order + QD + Dyn + QTF	60°
LC7	1st Order + QD + Dyn + QTF	90°

1st Order: first order potential flow theory; QTF: quadratic transfer function; QS: quasi-static mooring model; Dyn: dynamic mooring model.

The numerical data compared in this study were obtained by employing the code FAST (Fatigue, Aerodynamics, Structures, and Turbulence) [6,19,20] developed by NREL and the UOU in-house codes [16,21]. The hydrodynamic coefficients, including added mass, radiation damping and wave exciting forces, of the DeepCwind semi-submersible FOWT are obtained by using a diffraction/radiation solver in the frequency domain. Subsequently, the obtained hydrodynamic and wave loading data from the UOU in-house codes are fed into FAST as a platform loading output. Both of the hydrostatic and quadratic damping forces can be calculated in the UOU in-house codes. In addition, UOU's mooring quasi-static code uses the 4th order Runge–Kutta method to solve quasi-static equations of two dimensions of a mooring line.

In our simulation, the linearized potential-flow hydrodynamic radiation and diffraction problems in the frequency domain were first solved by using the three-dimensional panel method. The hydrodynamic coefficients and wave loading data were then transformed to time domain forms by the Cummins time domain equation as a system loading input. In addition, the quadratic transfer function (QTF) matrices with different frequencies and directions are deduced based on the near field integration over the mean wetted hull surface. In order to discuss the influences of mooring forces on the FOWT system, both of the quasi-static mooring model and the dynamic mooring model were considered in this study.

4.4. The Effect of Quadratic Damping

The hydrodynamic viscous damping plays a dominant role in the total hydrodynamic damping force for the DeepCwind semi-submersible FOWT. However, additional damping, namely quadratic damping, is required to accurately represent the damping in a real system for modeling potential flow without hydrodynamic viscous damping elements. Therefore, the quadratic damping matrix B [22] in Equation (35) can be used to represent potential flow theory that captures the effects of this viscous damping. The elements in Table 4 indicate the required quadratic viscous drag coefficient needed to match the simulation Morison viscous drag coefficients.

Table 4. Elements of quadratic damping matrix.

Mode	Surge	Sway	Heave	Roll	Pitch	Yaw
B_i (Unit)	1.25E6 (Ns^2/m^2)	0.95E6 (Ns^2/m^2)	3.88E6 (Ns^2/m^2)	3.35E10 (Nms^2/rad^2)	3.35E10 (Nms^2/rad^2)	1.15E10 (Nms^2/rad^2)

B_i denotes the i-th mode of the quadratic damping value.

Figure 11a–c present the RAOs in the surge, heave and pitch modes by comparing our simulation results of LC1 and LC2 with the UOU data in [23]. In the surge mode, there is little difference between our simulation results and the UOU data. On the other hand, it appears that the quadratic damping has a tiny effect on the surge RAO of the DeepCwind semi-submersible FOWT. In terms of the resonance peak in the heave mode, the quadratic damping has a considerable contribution to the heave RAO. It is clearly found that the heave RAO obtained from LC2 agrees well with the UOU data. However, the UOU's simulation estimates lower pitch motion than the result of LC2 and LC1. Generally, our simulation result of LC2 is in good agreement with the UOU data.

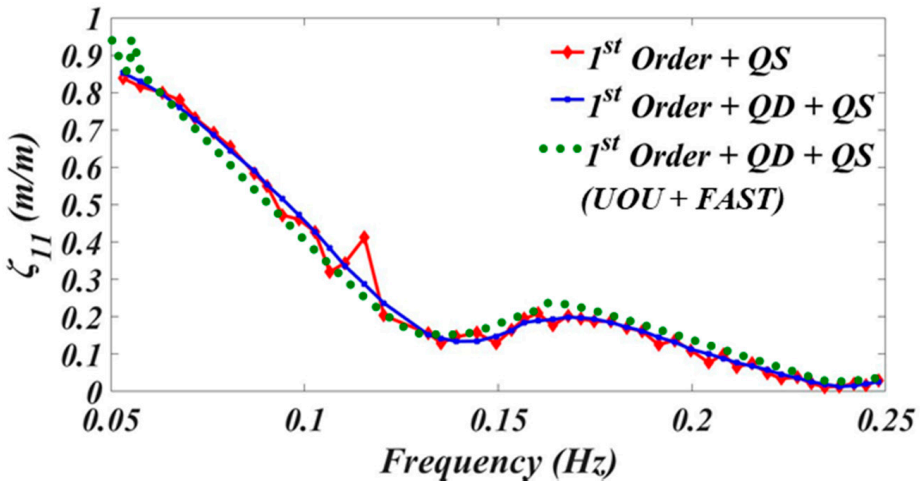

(**a**)

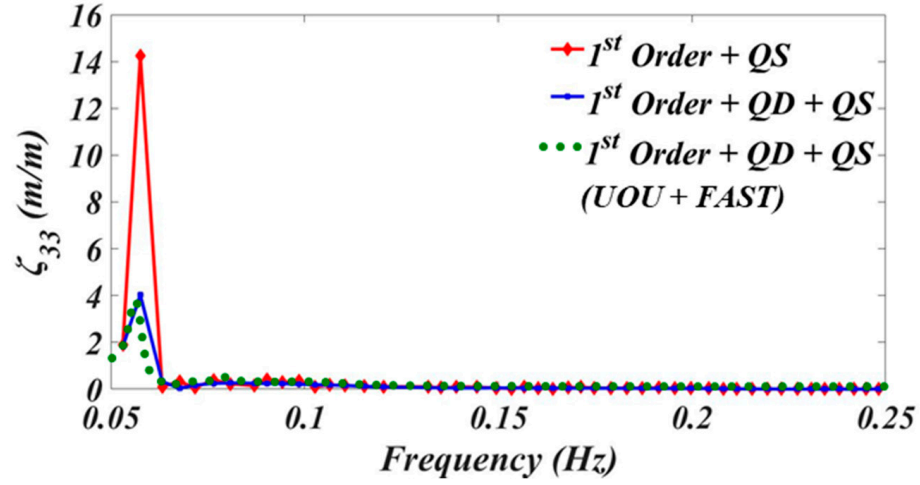

(**b**)

Figure 11. *Cont.*

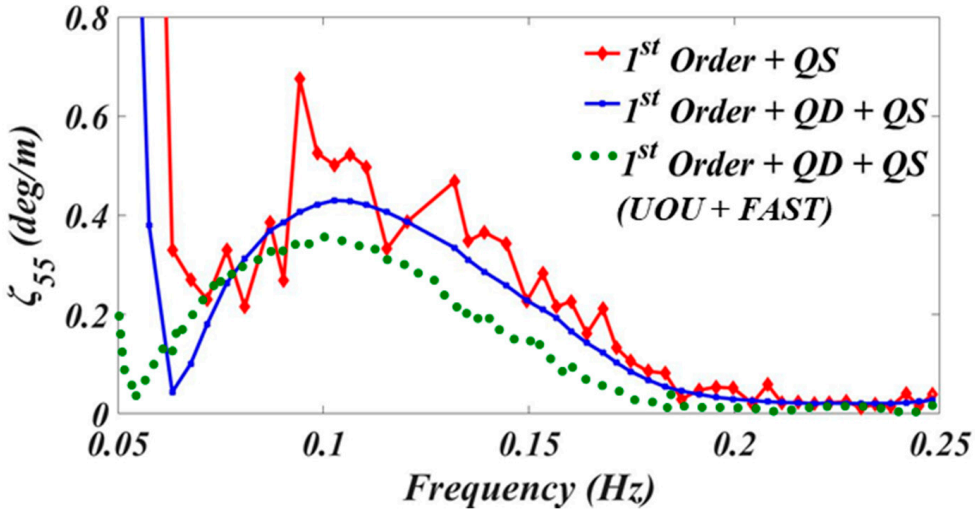

(**c**)

Figure 11. The effect of quadratic damping on (**a**) the surge, (**b**) the heave, and (**c**) the pitch modes, respectively.

4.5. The Effect of the Second-Order Wave Exciting Force

Since the 2nd order wave exciting force, namely the QTF, may have great influence on the platform motion and the mooring line tension [24], the 2nd order potential flow theories were used for calculating linear and nonlinear wave effects. The resonances of 2nd order wave exciting forces at the difference frequencies, i.e., the slow-drift wave forces, usually occur in the surge, sway and yaw modes; whereas the ones at the sum frequencies can only excite the heave, pitch and roll modes of the tension leg platform (TLP).

Figure 12a–f present the 6-DOF motion responses of the DeepCwind semi-submersible FOWT in the frequency domain by comparing LC3 with LC2. It is obvious that the sum-frequency force components have insignificant effects on the 6-DOF motion responses and then can be ignored. On the other hand, the slow-drift wave forces are found to have great contributions to the horizontal motion responses in the surge, sway, and yaw modes, but have little influence on the vertical motion responses in the heave, roll and pitch modes.

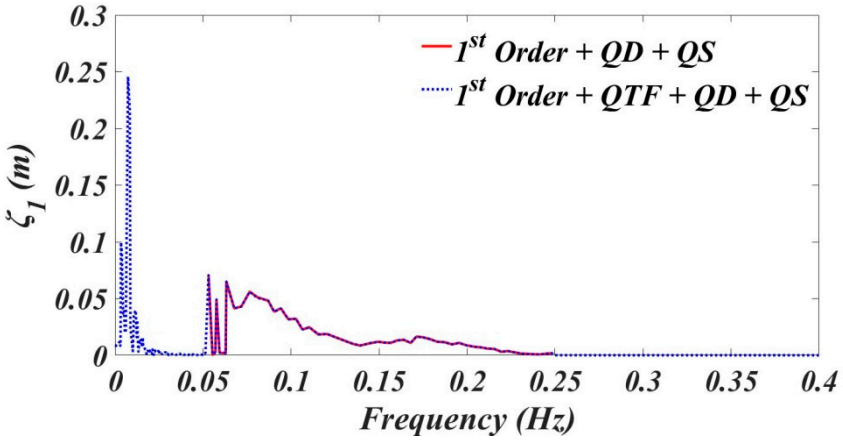

(**a**)

Figure 12. *Cont.*

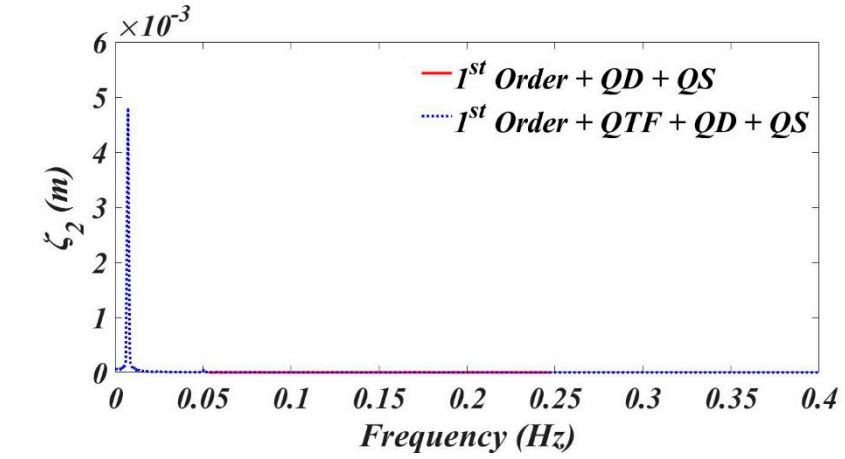

(**b**)

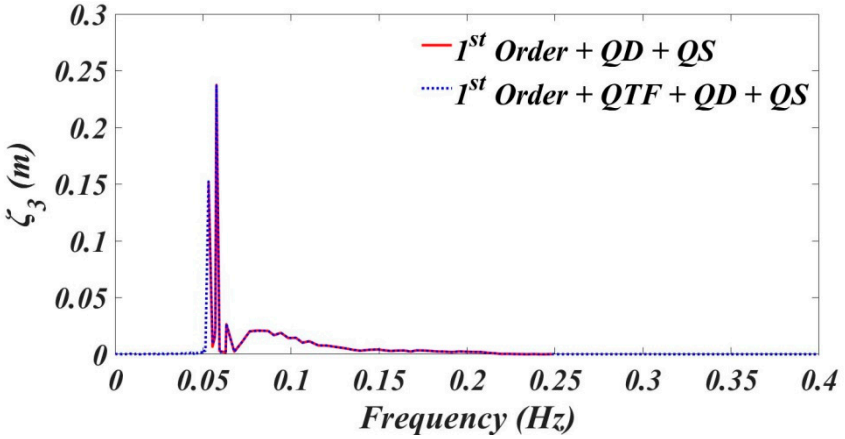

(**c**)

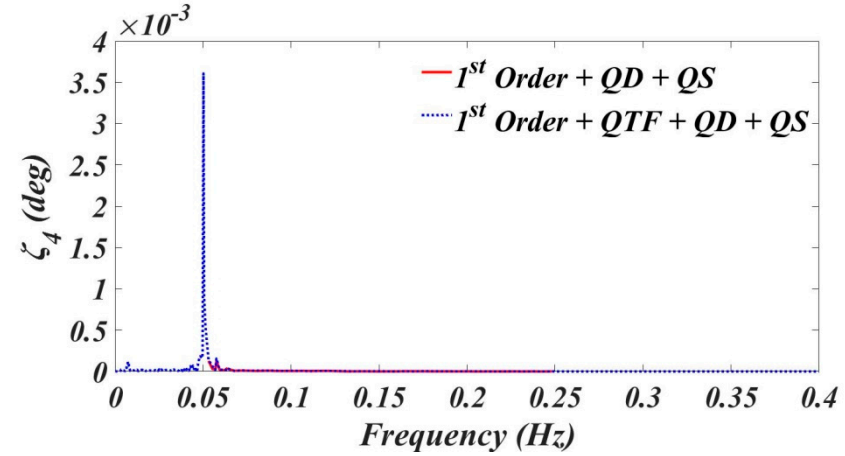

(**d**)

Figure 12. *Cont.*

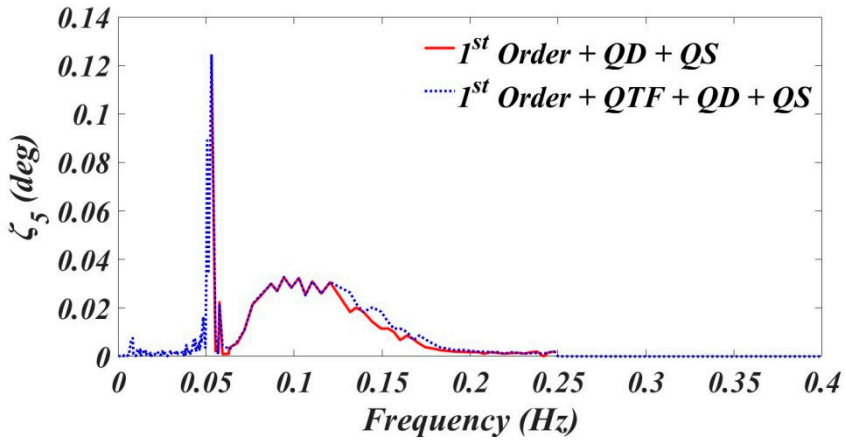

(e)

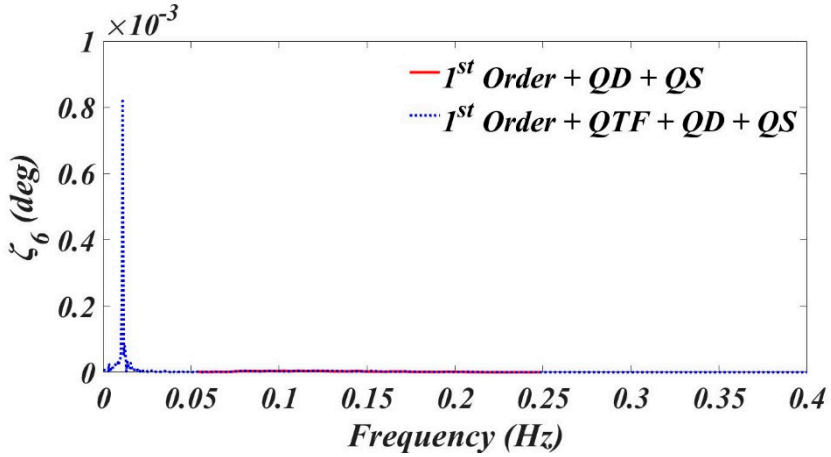

(f)

Figure 12. The effects of the QTFs on the motion responses in (**a**) the surge, (**b**) the sway, (**c**) the heave, (**d**) the roll, (**e**) the pitch, and (**f**) the yaw modes, respectively.

4.6. The Effect of Mooring Model

The quasi-static mooring model based on the MSQS approach is an efficient and simple approach for integrating into FOWT simulation. However, the major disadvantage is that the computation of the MSQS approach ignores the effects of hydrodynamic forces and inertial forces on the mooring cables, which are highly correlated with the platform motion and are therefore important for estimating the mooring forces. The main feature of the dynamic mooring model based on the LM approach can be used to discretize the behaviors of mooring cables. For comparison, the platform hydrodynamic forces, including the 2nd order wave exciting force and the quadratic viscous drag, would be coupled with both of the quasi-static and the dynamic mooring models.

Figure 13a–f present the 6-DOF motion responses of the DeepCwind semi-submersible FOWT in the frequency domain by comparing LC4 with LC3. As can be seen, there are small discrepancies of 6-DOF motion responses between the quasi-static model and the dynamic mooring model. However, portions of fairlead tension responses in Figure 14a–c indicate that the MSQS approach predicts reduced tensions compared to the LM approach. Masciola et al. [24] suggested that the platform motions were affected by the mooring dynamics only in harsh sea states but the mooring dynamics played a significant role in predicting the mooring loads in any sea condition. Our simulation results of the DeepCwind semi-submersible FOWT are evidently in good agreement with their findings.

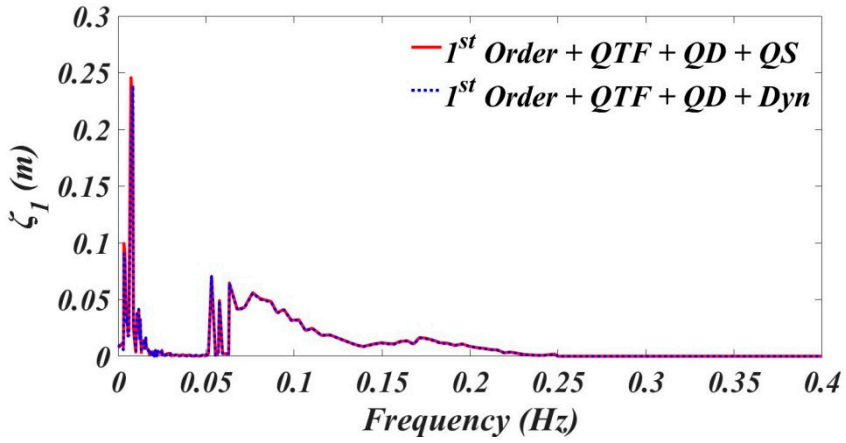

(a)

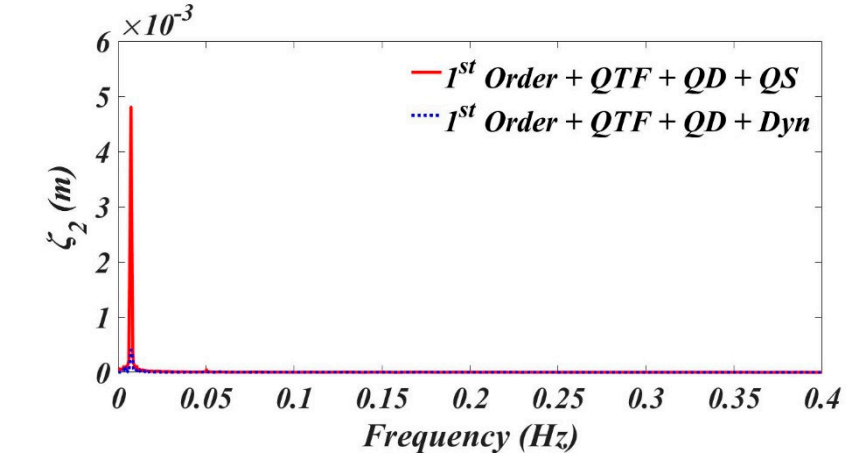

(b)

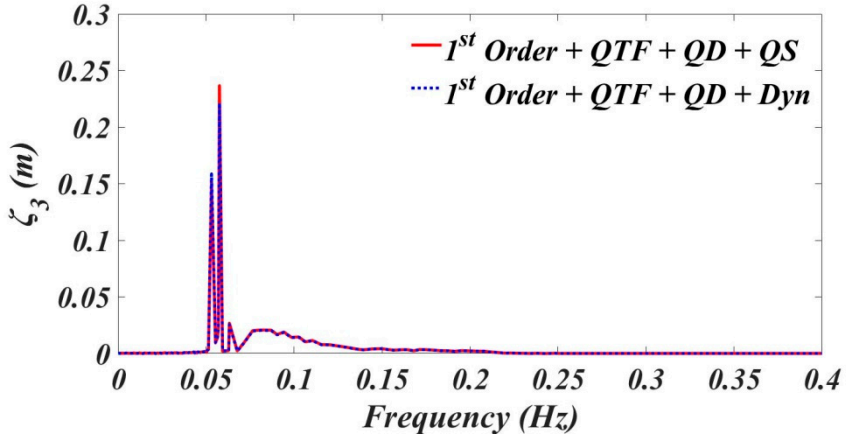

(c)

Figure 13. *Cont.*

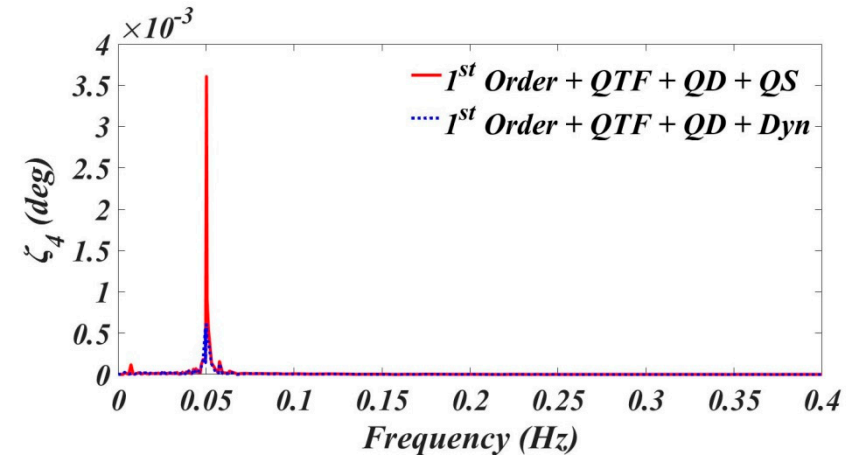

(**d**)

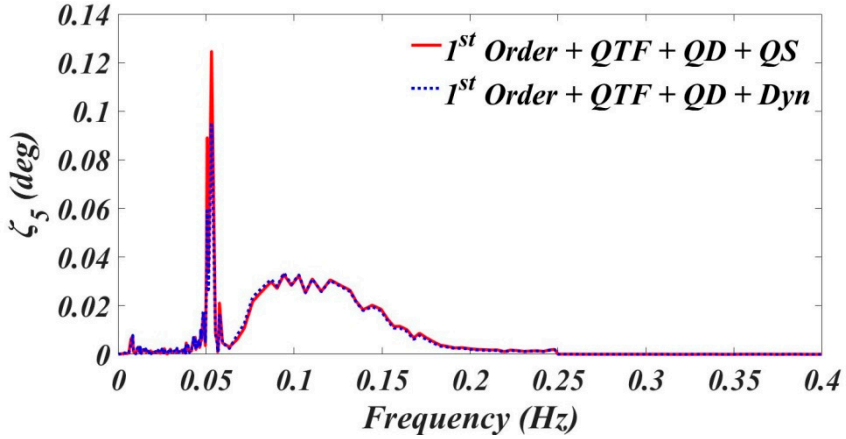

(**e**)

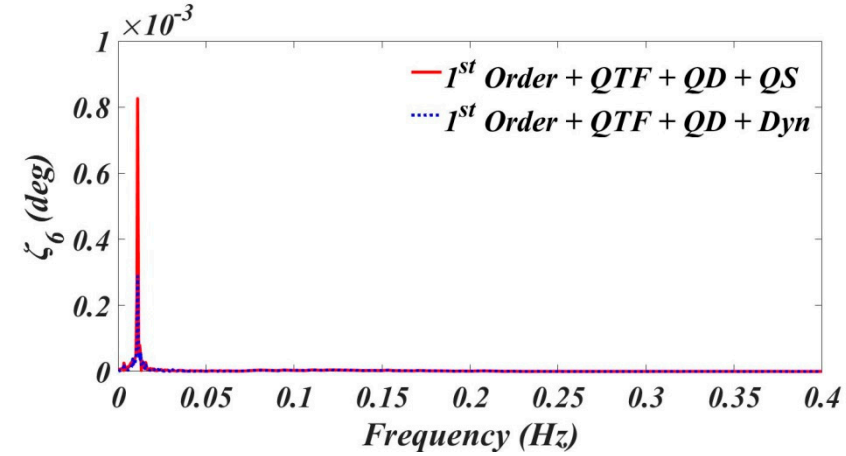

(**f**)

Figure 13. The effects of the mooring models on the motion responses in (**a**) the surge, (**b**) the sway, (**c**) the heave, (**d**) the roll, (**e**) the pitch, and (**f**) the yaw modes, respectively.

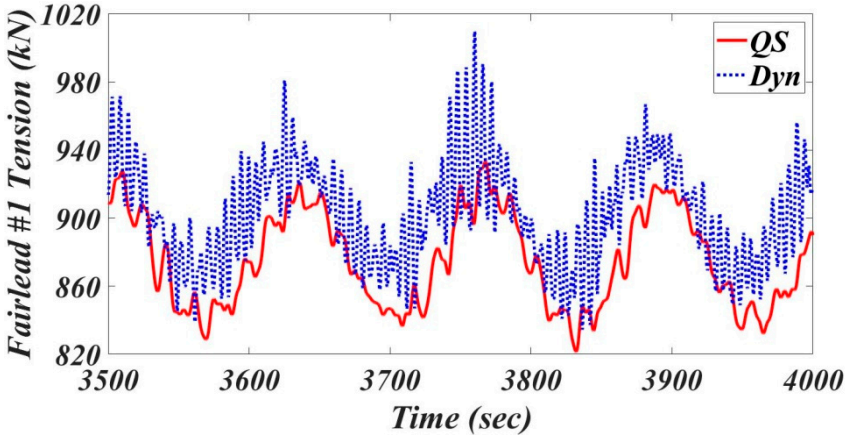

(a)

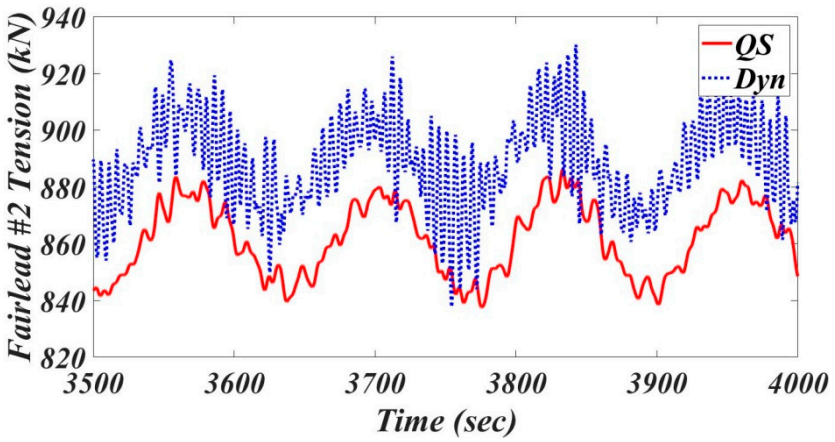

(b)

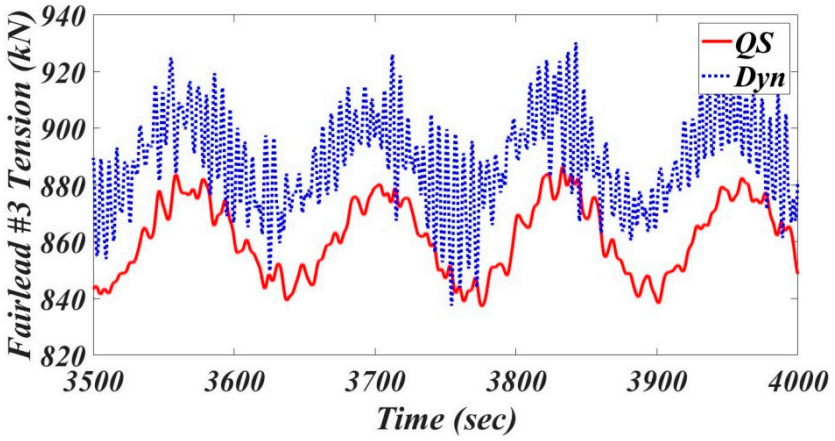

(c)

Figure 14. Time series of fairlead tension responses for the mooring cables: (**a**) #1, (**b**) #2, and (**c**) #3, respectively.

4.7. The Effect of Wave Heading Angle

Figure 15a–f exhibit the 6-DOF motion responses of the DeepCwind semi-submersible FOWT in the frequency domain at different wave heading angles for cases LC4–7. Due to the geometry symmetry of the DeepCwind semi-submersible FOWT, the heave motions appear to have the same magnitudes among all cases of varying wave heading angles. In contrast to the sway motion, it is evident that

the surge motion has the reduced amplitude response with the increase of the wave heading angle. Meanwhile, it is seen that the slow-drift force in the sway mode at 90° is more dominant than that in the surge mode at 0°. For the rotational modes, both of the roll and yaw motions have large responses with the increase of the wave heading angle in contrast to the results of the pitch motion. When the wave heading angle is changed, the surge, sway and yaw motions are more easily subject to the slow-drift forces than the other three motions.

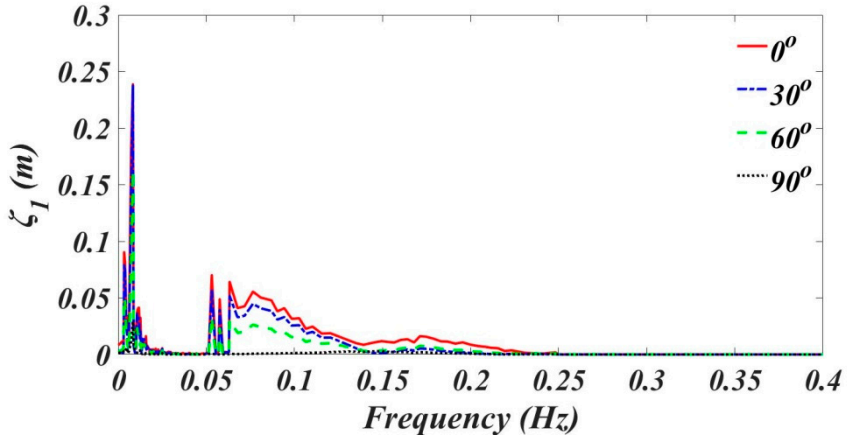

(**a**)

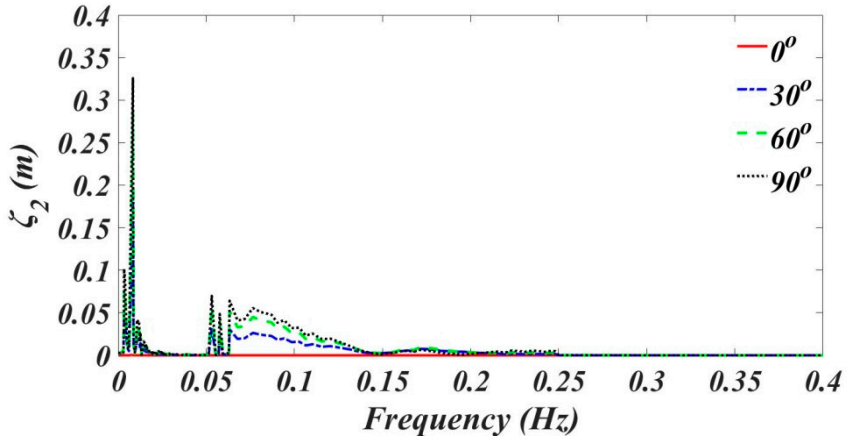

(**b**)

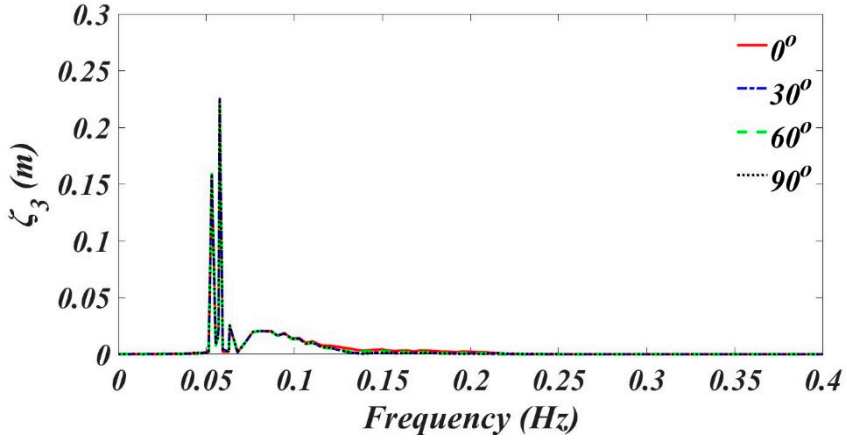

(**c**)

Figure 15. *Cont.*

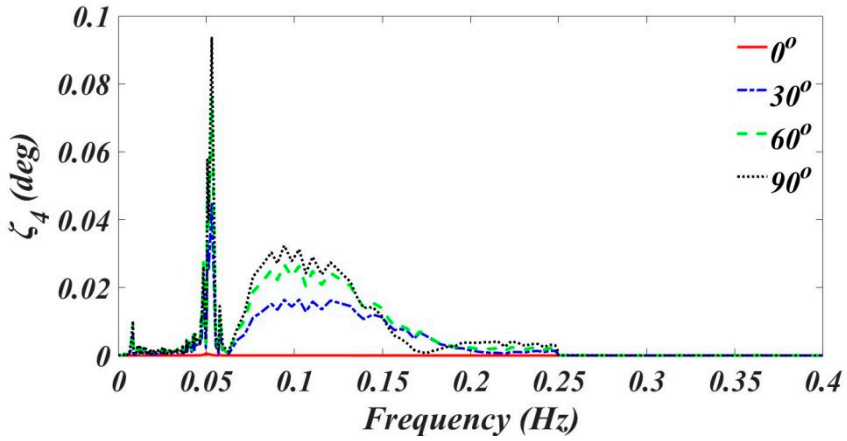

(**d**)

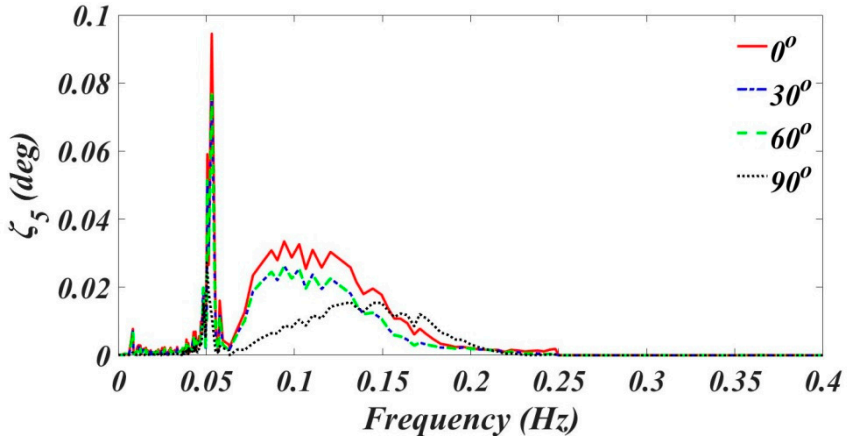

(**e**)

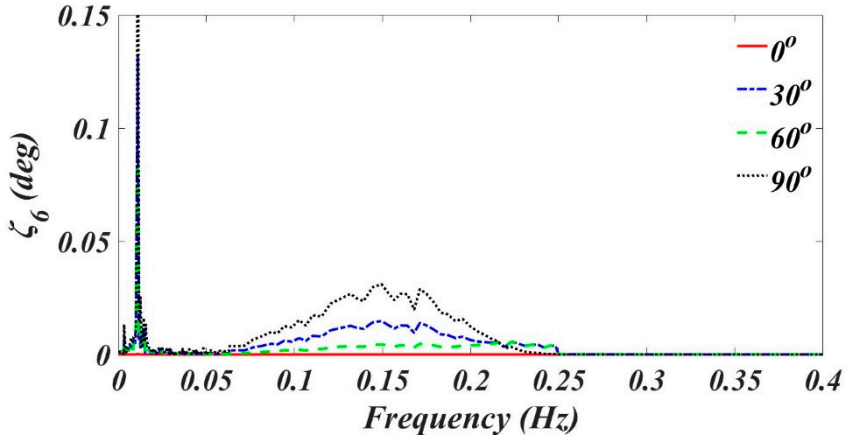

(**f**)

Figure 15. The effects of the wave heading angles on the motion responses in (**a**) the surge, (**b**) the sway, (**c**) the heave, (**d**) the roll, (**e**) the pitch, and (**f**) the yaw modes, respectively.

5. Conclusions

The hydrodynamic simulation of the DeepCwind semi-submersible FOWT discretized by the 3D panel method was discussed by considering the effects of the QTF and the quadratic damping

coupled with two different kinds of mooring models for varying wave heading angles. According to the simulation results, there are some concluding remarks that can be described as follows:

1. By mean of the grid-independence test, the simulation results of hydrodynamic coefficients for the semi-submersible FOWT are generally in good agreement with the ones by the WAMIT.
2. In addition to agreeing well with the UOU data, it is found that the quadratic damping has the most considerable contribution to the computation of the heave RAO compared with the surge and the pitch RAOs.
3. According to the analysis of the slow-drift wave forces, the QTFs are found to have great contributions to the horizontal motion responses in the surge, the sway, and the yaw modes, but have little influence on the vertical motion responses in the heave, the roll and the pitch modes.
4. Regarding the mooring effect, the 6-DOF motion responses in the frequency domain indicate that the estimation of the MSQS approach is close to the result of the LM approach. Nevertheless, the LM approach predicts more evident tension responses than the MSQS approach.
5. The variation of the wave heading angles has a tiny influence on the heave motion, whereas it is highly correlated with the slow-drift forces in the surge, the sway, and the yaw modes.
6. In a future study, the damage cases of a broken mooring line and the flooding of a single column will be considered to investigate system behaviors in extreme sea states.

Author Contributions: Y.-H.L. is the principal investigator and C.-H.Y. is the research assistant in this project. All authors have read and agreed to the published version of the manuscript.

Funding: This research received no external funding.

Acknowledgments: The authors would like to express their thanks to the Ministry of Science and Technology for a grant under Contract No. MOST 108-2221-E-006-120.

Conflicts of Interest: The authors declare no conflict of interest.

References

1. Bilgili, M.; Yasar, A.; Simsek, E. Offshore wind power development in Europe and its comparison with onshore counterpart. *Renew. Sustain. Energy Rev.* **2011**, *15*, 905–915. [CrossRef]
2. Esteban, M.D.; Diez, J.J.; López, J.S.; Negro, V. Why offshore wind energy? *Renew. Energy* **2011**, *36*, 444–450. [CrossRef]
3. Butterfield, S.; Musial, W.; Jonkman, J.; Sclavounos, P. *Engineering Challenges for Floating Offshore Wind Turbines*; National Renewable Energy Lab. (NREL): Golden, CO, USA, 2007.
4. Newman, J.N. *Marine Hydrodynamics*; MIT Press: Cambridge, MA, USA, 2018.
5. Borg, M.; Collu, M.; Kolios, A. Offshore floating vertical axis wind turbines, dynamics modelling state of the art. Part II: Mooring line and structural dynamics. *Renew. Sustain. Energy Rev.* **2014**, *39*, 1226–1234. [CrossRef]
6. Jonkman, J.M. *Dynamics Modeling and Loads Analysis of an Offshore Floating Wind Turbine*; National Renewable Energy Lab. (NREL): Golden, CO, USA, 2007.
7. Thomsen, J.B.; Ferri, F.; Kofoed, J.P. Experimental testing of moorings for large floating wave energy converters. In Proceedings of the Progress in Renewable Energies Offshore: Proceedings of the 2nd International Conference on Renewable Energies(RENEW2016), Lisbon, Portugal, 24–26 October 2016.
8. Masciola, M.; Jonkman, J.; Robertson, A. Implementation of a multisegmented, quasi-static cable model. In Proceedings of the Twenty-Third International Offshore and Polar Engineering Conference, Anchorage, AK, USA, 30 June–5 July 2013.
9. Hall, M.; Goupee, A. Validation of a lumped-mass mooring line model with DeepCwind semisubmersible model test data. *Ocean Eng.* **2015**, *104*, 590–603. [CrossRef]
10. Lin, Y.-H.; Kao, S.-H.; Yang, C.-H. Investigation of Hydrodynamic Forces for Floating Offshore Wind Turbines on Spar Buoys and Tension Leg Platforms with the Mooring Systems in Waves. *Appl. Sci.* **2019**, *9*, 608. [CrossRef]

11. Robertson, A.; Jonkman, J.; Masciola, M.; Song, H.; Coupee, A.; Coulling, A.; Luan, C. *Definition of the Semisubmersible Floating System for Phase II of OC4*; Technical Report NREL, TP-5000-60601; National Renewable Energy Laboratory: Golden, CO, USA, 2014.
12. Pinkster, J.A. Low Frequency Second Order Wave Exciting Forces on Floating Structures. 1980. Available online: https://repository.tudelft.nl/islandora/object/uuid:d6d42e9c-c349-47e5-8d63-5c6454196b04?collection=research (accessed on 13 May 2020).
13. Hasselmann, K.; Barnett, T.; Bouws, E.; Carlson, H.; Cartwright, D.; Enke, K.; Ewing, J.; Gienapp, H.; Hasselmann, D.; Kruseman, P.; et al. Measurements of wind-wave growth and swell decay during the Joint North Sea Wave Project (JONSWAP). *Ergänzungsheft 8-12* **1973**.
14. DNV-RP. *C205 Environmental Conditions and Environmental Loads*; Det Norske Veritas: Oslo, Norway, 2010.
15. Cummins, W. *The Impulse Response Function and Ship Motions*; David Taylor Model Basin: Washington, DC, USA, 1962.
16. Kim, J.; Shin, H. Model test & numerical simulation of OC4 semi-submersible type floating offshore wind turbine. In Proceedings of the 26th International Ocean and Polar Engineering Conference, Rhodes, Greece, 26 June–2 July 2016.
17. Tran, T.T.; Kim, D.-H. The coupled dynamic response computation for a semi-submersible platform of floating offshore wind turbine. *J. Wind Eng. Ind. Aerodyn.* **2015**, *147*, 104–119. [CrossRef]
18. Robertson, A.; Jonkman, J.; Vorpahl, F.; Popko, W.; Qvist, J.; Froyd, L.; Chen, X.; Azcona, J.; Uzungoglu, E.; Guedes Soares, C.; et al. *Offshore Code Comparison Collaboration, Continuation within IEA Wind Task 30: Phase II Results Regarding a Floating Semisubmersible Wind System*; National Renewable Energy Lab. (NREL): Golden, CO, USA, 2014.
19. Jonkman, J.M.; Buhl, M.L., Jr. *FAST User's Guide*; National Renewable Energy Laboratory: Golden, CO, USA, 2005; p. 366.
20. Jonkman, J. Influence of control on the pitch damping of a floating wind turbine. In Proceedings of the 46th AIAA Aerospace Sciences Meeting and Exhibit, Reno, NV, USA, 7–10 January 2008; p. 1306.
21. Shin, H.; Kim, B.; Dam, P.T.; Jung, K. Motion of OC4 5MW semi-Submersible offshore wind turbine in irregular waves. In Proceedings of the ASME 2013 32nd International Conference on Ocean, Offshore and Arctic Engineering, Nantes, France, 9–14 June 2013.
22. Robertson, A.; Jonkman, J.; Vorpahl, F.; Popko, W.; Qvist, J.; Frøyd, L.; Chen, X.; Azcona, J.; Uzunoglu, E.; Guedes Soares, C.; et al. Offshore code comparison collaboration continuation within IEA wind task 30: Phase II results regarding a floating semisubmersible wind system. In Proceedings of the ASME 2014 33rd International Conference on Ocean, Offshore and Arctic Engineering, San Francisco, CA, USA, 8–13 June 2014.
23. Chuang, Z.; Liu, S.; Lu, Y. Influence of second order wave excitation loads on coupled response of an offshore floating wind turbine. *Int. J. Nav. Archit. Ocean Eng.* **2020**, *12*, 367–375. [CrossRef]
24. Masciola, M.; Robertson, A.; Jonkman, J.; Coulling, A.; Goupee, A. Assessment of the importance of mooring dynamics on the global response of the DeepCwind floating semisubmersible offshore wind turbine. In Proceedings of the 23rd International Offshore and Polar Engineering Conference, Anchorage, AK, USA, 30 June–4 July 2013.